

Evidence for Exciton Crystals in a 2D Semiconductor Heterotrilinear

Yusong Bai,¹ Song Liu,² Yinjie Guo,³ Jordan Pack,³ Jue Wang,¹ Cory R. Dean,³ James Hone,² X.-Y. Zhu^{1,*}

1. Department of Chemistry, Columbia University, New York, NY 10027, USA.
2. Department Mechanical Engineering, Columbia University, New York, NY 10027, USA.
3. Department of Physics and Astronomy, Columbia University, New York, NY, 10027, USA.

Two-dimensional (2D) transition metal dichalcogenides (TMDC) and their moiré interfaces have been demonstrated for correlated electron states, including Mott insulators and electron/hole crystals commensurate with moiré superlattices¹⁻⁷. Here we present spectroscopic evidences for ordered bosons - interlayer exciton crystals in a WSe₂/MoSe₂/WSe₂ trilayer, where the enhanced Coulomb interactions over those in heterobilayers have been predicted to result in exciton ordering⁸⁻¹⁰. While the dipolar interlayer excitons in the heterobilayer may be ordered by the periodic moiré traps¹¹⁻¹⁴, their mutual repulsion results in de-trapping at exciton density $n_{\text{ex}} \geq 10^{11} \text{ cm}^{-2}$ to form mobile exciton gases and further to electron-hole plasmas, both accompanied by broadening in photoluminescence (PL) peaks and large increases in mobility¹⁵. In contrast, ordered interlayer excitons in the trilayer are characterized by negligible mobility and by sharper PL peaks persisting to $n_{\text{ex}} \geq 10^{12} \text{ cm}^{-2}$. We find that an optically dark state attributed to the predicted quadrupolar exciton crystal transitions to the bright dipolar excitons either with increasing n_{ex} or by an applied electric field. These ordered interlayer excitons may serve as models for the exploration of quantum phase transitions and quantum coherent phenomena.

Fermions and bosons can undergo quantum phase transitions and form ordered ground states. These processes are determined by changes to fundamental parameters in the system Hamiltonian¹⁶ rather than temperature in the more familiar thermal phase transitions. TMDC homo- and hetero-bilayers have emerged as model systems for the realization of ordered electron states. The reduced screening can give rise to strong many-body Coulomb potential dominating

* To whom correspondence should be addressed: xyzhu@columbia.edu

over the carrier kinetic energy, which is intrinsically low in these systems and is further lowered by moiré band flattening, leading to ordered fermions¹⁻⁷. In contrast, experimental realization of the ordering of the bosonic excitons in 2D has remained a challenge¹⁷. Interlayer excitons in TMDC heterojunctions with type-II band alignment may offer a platform for realizing ordered excitons. The spatial separation of the electron-hole pair results in long exciton lifetimes (10^2 ns) which in turn permits broad tuning of exciton density under continuous-wave (CW) optical excitation¹⁸. The large out-of-plane dipole moments enable long-range Coulomb interaction, a key ingredient in Wigner crystal formation¹⁹ from their Fermionic counterparts. The presence of moiré pattern can also flatten the electron/hole bands^{20,21} and introduce potential traps to localize interlayer excitons²², thus reducing exciton kinetic energy and facilitating crystallization. Despite these favorable conditions, interlayer exciton crystals in TMDC heterobilayers have not been observed to date.

Interestingly, recent theoretical studies predicted that increasing the thickness from an asymmetric heterobilayer to a symmetric heterotrilayer (e.g., $\text{WSe}_2/\text{MoSe}_2/\text{WSe}_2$) results in the formation of robust crystalline phases of exciton⁸⁻¹⁰. Fig. 1a illustrates the calculated band structures⁸ for $\text{MoSe}_2/\text{WSe}_2$ and $\text{WSe}_2/\text{MoSe}_2/\text{WSe}_2$. In the latter, there is an additional valence band splitting (Δ_\pm) in the K valley due to hole-hopping between the two WSe_2 layers. As a result, the interlayer exciton is quadrupolar (IX^{Δ_Q}) and can be considered as consisting of 0.5 hole each in the top and bottom WSe_2 layer and one electron in the middle MoSe_2 layer. A quadrupolar exciton is stabilized over a dipolar exciton ($\text{IX}^{\text{u(d)}}$) by $\Delta_Q = \frac{1}{2}\Delta_\pm \sim -20 \pm 10$ meV, which is termed the “quantum fluctuation” energy⁸. Following Slobodkin et al.⁸, we write the many-body Hamiltonian of interlayer excitons in the $\text{WSe}_2/\text{MoSe}_2$ heterobilayer as:

$$\hat{H}_{BL} = \sum_i (K_i) + \sum_{i < j} V_{\uparrow_i \uparrow_j} \quad (1),$$

where K_i the exciton kinetic energy operator, $V_{\uparrow_i \uparrow_j}$ is the Coulomb repulsion between parallelly ($\uparrow_i \uparrow_j$) aligned dipoles. The short-range exchange interaction due to Fermionic characters of the charge separated excitons is neglected at low densities. For the symmetric $\text{WSe}_2/\text{MoSe}_2/\text{WSe}_2$ heterotrilayer, the Hamiltonian becomes:

$$\hat{H}_{TL} = \sum_i (K_i) + \sum_{i < j} (V_{\uparrow_i \uparrow_j} - V_{\uparrow_i \downarrow_j}) - \Delta_Q \sum_i \sigma_i^x \quad (2).$$

where the additional $-V_{\uparrow_i\downarrow_j}$ accounts for Coulomb attraction when two interlayer excitons anti-parallelly ($\uparrow_i\downarrow_j$) aligned in the top and bottom heterobilayer, respectively; the last term is the quadrupolar exciton stabilization energy and the σ_i^x operator flips each dipole.

The additional two stabilization terms in the heterotrilaier are essential to the formation of robust interlayer exciton crystals, shown in the phase diagram in Fig. 1b. Here, the competition between Δ_Q and the Coulomb energy $U \propto \frac{e^2}{\epsilon d}$ (e : electron charge, ϵ : dielectric constant, d : interlayer spacing) is represented by a unitless parameter $R = \frac{\Delta_Q}{U}$. For the specific WSe₂/MoSe₂/WSe₂ trilaier system⁸, R is estimated to be above R_c , and quadrupolar excitons adopting a triangular lattice is the lowest energy state at exciton density $n_{\text{ex}} < 10^{13} \text{ cm}^{-2}$. Increasing n_{ex} results in a phase transition to the staggered dipolar excitons in a square lattice where Coulomb attraction dominates. For low R values, staggered dipolar exciton droplets may also form at low n_{ex} . Note that the predicted exciton lattices illustrated in Fig. 1b differ from the recently reported exciton insulators^{23,24} in a TMDC moiré bilayer separated from a TMDC monolayer or exciton density waves²⁵ in a double TMDC moiré bilayer with weak inter-moiré layer coupling. In these systems, the correlation effect is likely rooted in the Mott physics of the electron/hole residing in the moiré structure.

Here we report spectroscopic evidences for the predicted exciton crystals and quantum phase transitions in the WSe₂/MoSe₂/WSe₂ trilaier. We fabricate the WSe₂/MoSe₂/WSe₂ heterostructure with an extra WSe₂/MoSe₂ bilayer region as control using the highest quality WSe₂ and MoSe₂ monolayers²⁶ and the transfer stacking technique detailed elsewhere¹ (see Methods Figs. S1-S5). A schematic of the structure is shown in Fig. 1c and an optical image in Fig. 1d. The three TMDC monolayers are at near-zero twist angles ($< 1^\circ$) as characterized by phase-resolved second-harmonic-generation (SHG). At such a small twist angle, the moiré unit cell density is $n_{\text{moiré}} \leq 3.2 \times 10^{11} \text{ cm}^{-2}$. We adopt a dual-gate architecture with hexagonal boron nitride (h-BN) encapsulation and semitransparent graphene (3-4 layers) top (V_{tg}) and bottom (V_{bg}) gate electrodes; this allows us to independently control the out-of-plane electric field and electrostatic doping of the heterostructure without losing optical access (Methods). We probe the exciton phases in the trilaier via PL spectroscopy. The near-perfect angular alignments satisfy electron-hole momentum-matching conditions for optical transitions²⁷. Fig. 1e compares PL spectra at zero

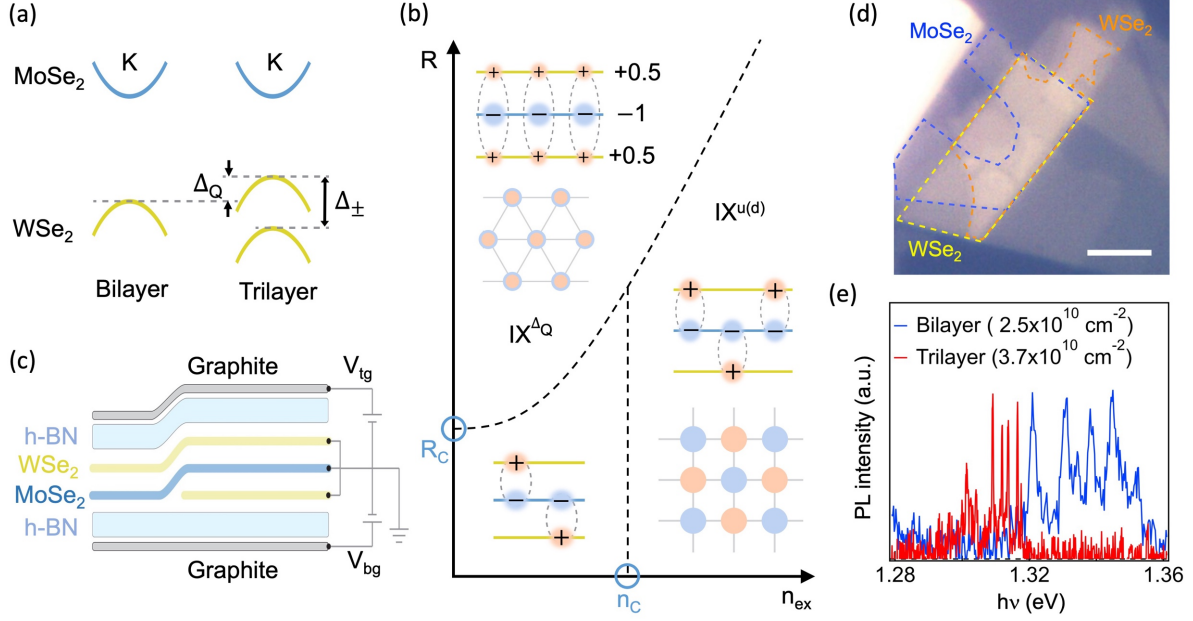


Fig. 1 | The WSe₂/MoSe₂/WSe₂ trilayer: energetics, excitonic phases, and device architectures. (a) Band structure of the WSe₂/MoSe₂ bilayer and the WSe₂/MoSe₂/WSe₂ trilayer. Δ_{\pm} is the hole-hopping-induced band splitting and $\Delta_Q = \frac{1}{2}\Delta_{\pm}$ is the energy difference between the valence band edges of the bilayer and the trilayer. (b) Schematic phase diagram of interlayer excitons in WSe₂/MoSe₂/WSe₂. n_{ex} is the exciton density and R ($= \frac{\Delta_Q}{U}$; U , the Coulomb interaction) is a dimensionless parameter. $IX^{\Delta Q}$: the quadrupolar interlayer exciton crystal; $IX^{u(d)}$: the anti-parallel interlayer excitons with dipole moments pointing upward (u) or downward (d). (c) Schematic of the device. V_{tg} and V_{bg} are the top- and bottom-gate voltages for independent control over electric field and electrostatic doping. (d) An optical image of the WSe₂/MoSe₂/WSe₂ heterostructure in top view. Scale bar is 10 μm . A larger image is in Fig. S5. (e) PL spectra of interlayer excitons from the WSe₂/MoSe₂ bilayer (orange) and the WSe₂/MoSe₂/WSe₂ trilayer (blue) at $V_{tg} = V_{bg} = 0$ V; CW excitation, $h\nu = 2.33$ eV; calibrated exciton density $n_{ex} = 3.0 \times 10^{11} \text{ cm}^{-2}$ and $3.9 \times 10^{11} \text{ cm}^{-2}$ for the bilayer and trilayer, respectively; Sample temperature $T = 4.6$ K.

electric field and gate-doping ($V_{tg} = V_{bg} = 0$) and low excitation densities, $n_{ex} = 2.5 \times 10^{10}$ and $3.7 \times 10^{10} \text{ cm}^{-2}$, for the bilayer and trilayer, respectively. Calibration of exciton densities can be found in Supporting Information and Fig. S6-S8. Each spectrum in Fig. 1e consists of a distribution of narrow peaks in the interlayer exciton energy range. In the bilayer region, the sharp PL peaks with full-width-at-half-maximum (FWHM) of 1.0 ± 0.2 meV result from interlayer excitons in the quantum-emitter like moiré traps^{11,13,28} with photon antibunching characteristics²⁹, and variations in peak energy may be attributed to dielectric disorder. In the trilayer, the PL peaks are five-times sharper with $\text{FWHM} = 0.20 \pm 0.05$ meV. The sharp PL peaks in the trilayer persists to n_{ex} much higher than they do in the bilayer, as detailed below.

Robust exciton crystals and phase transitions in the trilayer. The n_{ex} dependent PL spectra provide evidence for the predicted exciton crystals in the trilayer. As comparison, we first present PL spectra from the WSe₂/MoSe₂ bilayer in a pseudo-color plot in Fig. 2a and at selected n_{ex} in Fig. 2b. At the lowest n_{ex} , the spectra feature a group of narrow peaks corresponding to moiré trapped excitons^{11,13,28,29}. Above $\sim 1 \times 10^{11} \text{ cm}^{-2}$, the peaks broaden and merge due to transition to the free exciton gas¹⁵; further broadening occurs upon transition to plasmas near and above the Mott density ($\sim 3 \times 10^{12} \text{ cm}^{-2}$), in agreement with previous studies^{11,13,15}. The n_{ex} -dependent PL spectra from the WSe₂/MoSe₂/WSe₂ trilayer, Fig. 2c & 2d, are distinct. The first distinction is the extreme robustness of the sharp exciton peaks persisting to n_{ex} in the 10^{12} cm^{-2} region. This is more obvious in the peak intensity normalized PL spectra in Fig 2e. The peak positions and FWHMs remain nearly constant to $n_{\text{ex}} \sim 5 \times 10^{12} \text{ cm}^{-2}$, which is approximately the Mott density. These results

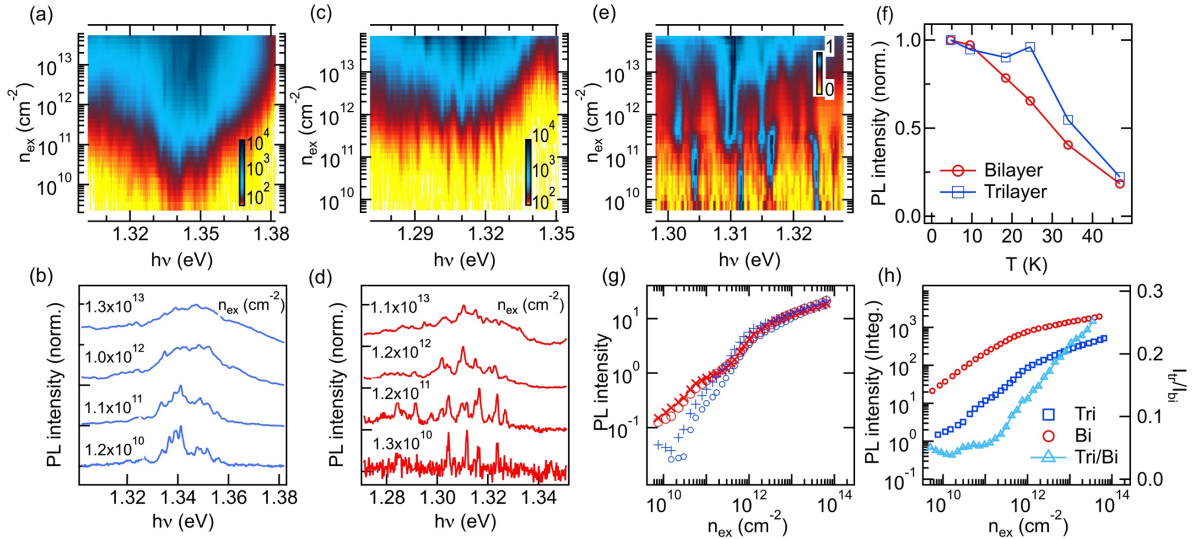


Fig. 2 | Density-dependent PL spectra suggest robust interlayer exciton crystals in the trilayer. (a) PL spectra as a function of excitation power (ρ) from interlayer excitons in the WSe₂/MoSe₂ bilayer. Color scale is PL intensity; (b) ρ -dependent PL spectra from interlayer excitons in the WSe₂/MoSe₂/WSe₂ trilayer. Note the PL intensity is scaled by $\times 5$ for $\rho \leq 0.3 \mu\text{W}$. (c) The same spectra as in (b), but with PL intensity normalized to peak value at each ρ value. (d) ρ -dependent PL peak energies (orange) and FWHM (blue) for two PL peaks in (b) at 1.3015 eV (triangles) and 1.3098 eV (circles); (e) Temperature-dependent PL intensity for interlayer excitons in the WSe₂/MoSe₂ bilayer (red circles) and the WSe₂/MoSe₂/WSe₂ (blue squares) at $\rho = 0.1 \mu\text{W}$; (f-g) ρ -dependent PL peak intensity for two pairs of peaks in (b) at 3.001 eV (blue) / 3.004 eV (red) and 3.121 eV (blue) / 3.124 eV (red), respectively. (h) Integrated PL intensities as functions of ρ from the bilayer (I_{B} , red circles) and the trilayer (I_{T} , blue squares), respectively. Also shown in (h) is the ratio $I_{\text{T}}/I_{\text{B}}$ (right axis). CW excitation: $h\nu = 2.33 \text{ eV}$, sample temperature $T = 4.6 \text{ K}$, except in panel (e) where $T = 4.6 - 46 \text{ K}$.

suggest that crystal formation is more effective in spatially localizing the interlayer excitons and in preventing inter-exciton scattering than the moiré traps do. Supporting the stability of interlayer excitons in crystalline phases, we compare in Fig. 2f the temperature (T) dependences in integrated PL intensities at an excitation power of 0.5 μW , corresponding to $n_{\text{ex}} = 6.3 \times 10^{11} \text{ cm}^{-2}$ and $7.9 \times 10^{11} \text{ cm}^{-2}$ at 4 K for the bilayer and the trilayer, respectively. At this excitation power, the bilayer is dominated by interlayer excitons in the free exciton gas phase, and the PL intensity exhibits a rapid drop with increasing temperature. In contrast, the PL intensity remains nearly constant in the trilayer until a critical temperature of $T_c = 25 \text{ K}$ above which decay occurs. T_c is likely the thermal melting temperature of the exciton crystals. The FWHM of PL from the trilayer remain narrow until $T \sim 25 \text{ K}$ (Fig. S9-S10), consistent with the crystalline phases prior to thermal melting.

The second distinctive feature is the evolution of PL intensity with n_{ex} . At $n_{\text{ex}} \leq 2 \times 10^{11} \text{ cm}^{-2}$, the PL intensity from the trilayer is more than one-order of magnitude lower than that from the bilayer; this is consistent with the dominance of the optically dark nature of the predicted quadrupolar exciton lattice. The dark excitons are gradually switched bright with increasing n_{ex} above $2 \times 10^{11} \text{ cm}^{-2}$ (close to $n_{\text{moiré}}$), as is most evident in the peak-intensity normalized spectra in Fig. 3e where a clear onset for the brightening of a large portion of the excitons is seen. Fig. 3g compare as functions of n_{ex} the integrated PL intensities of two pairs of excitons at 1.301 eV/1.304 eV and 1.321 eV/1.324 eV, respectively. In each case, the intensity of the darker exciton (blue) catches up with that of the brighter ones at $n_{\text{ex}} > 2 \times 10^{11}$. The switching of dark-to-bright is also reflected in the n_{ex} dependences of PL intensity ratio between the trilayer and the bilayer, $I_{\text{tr}}/I_{\text{bi}}$, which remains constant ($= 0.065 \pm 0.005$) for $n_{\text{ex}} \leq 2 \times 10^{11} \text{ cm}^{-2}$ but increases continuously to ~ 0.25 at $n_{\text{ex}} \sim 3 \times 10^{13} \text{ cm}^{-2}$, Fig. 1h. This trend suggests the transition and continuous addition to the bright dipolar exciton crystal in the trilayer, i.e., it is compressible.

Immobile excitons in the crystalline phases. To determine the diffusivity of the interlayer excitons, we carry out confocal PL imaging under diffraction-limited and continuous wave (CW) excitation conditions¹⁵, where the generation, diffusion, and recombination of the excitons reach a steady state. Fig. 3a shows PL intensity images of interlayer excitons in the bilayer (upper) and trilayer (lower) at selected excitation powers (0.1-3 μW), corresponding to average excitation densities within the diffraction limited spots of $n_{\text{ex}} = 1.7 \times 10^{11} - 2.2 \times 10^{12} \text{ cm}^{-2}$ and $n_{\text{ex}} = 2.2 \times 10^{11} - 3.0 \times 10^{12} \text{ cm}^{-2}$ for the bilayer and trilayer, respectively. At the lowest n_{ex} , the Gaussian width (σ_{ex}) of the PL image in either the bilayer or the trilayer is close to that of the excitation spot $\sigma_0 \sim 0.4$

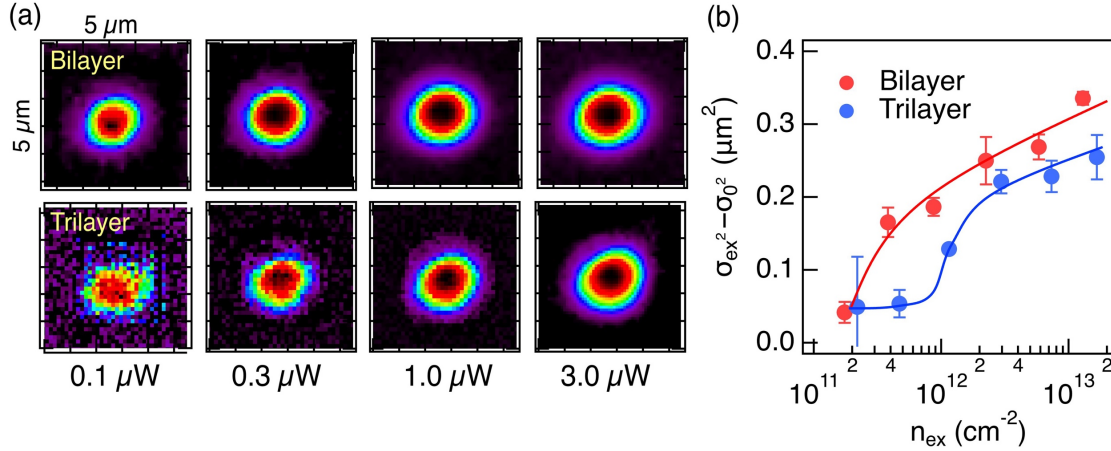


Fig. 3 | Steady-state diffusion of interlayer excitons in MoSe₂/WSe₂ heterobilayer and WSe₂/MoSe₂/WSe₂ trilayer. (a) Selected PL images at different CW excitation powers (0.3-3.0 μW) with a diffraction-limited excitation spot of Gaussian width $\sigma_0 \sim 0.5 \mu\text{m}$. Each image is $5 \times 5 \mu\text{m}^2$. (b) Excitation density (n_{ex}) dependent differential variance, $\Delta\sigma^2 = \sigma_{\text{ex}}^2 - \sigma_0^2$, where σ_{ex} and σ are the Gaussian widths of each PL image and the excitation spot, respectively. Red dots: bilayer; blue dots: trilayer. The red and blues curves serve as guides to the eye.

μm , suggesting negligible diffusivity of the interlayer excitons (see Supporting Information Fig. S11-S14). The Gaussian widths broaden with n_{ex} , but the trends are different for the two cases. Fig. 3b shows changes in the spatial variance of the PL images, $\Delta\sigma^2 = \sigma_{\text{ex}}^2 - \sigma_0^2$, as a function of n_{ex} . For interlayer excitons in the bilayer (red circles), $\Delta\sigma^2$ increases monotonically with n_{ex} , indicating increased diffusivity as the system transitions from moiré trapped interlayer excitons to free exciton gas and to electron-hole plasmas.¹⁵ In contrast, $\Delta\sigma^2$ remains negligible for $n_{\text{ex}} \leq 5 \times 10^{11} \text{ cm}^{-2}$ and increases at $n_{\text{ex}} \geq 1 \times 10^{12} \text{ cm}^{-2}$. The negligible diffusivity at $n_{\text{ex}} < 1 \times 10^{12} \text{ cm}^{-2}$ in the trilayer is consistent with the dominance of crystalline phases.

Field induced excitonic phase transitions in the trilayer. Further evidence of the exciton crystals comes from electric field (\vec{E}) dependences. Figs. 4a and 4b show \vec{E} -dependent PL spectra for the bilayer and trilayer at $n_{\text{ex}} = 3.0 \times 10^{11} \text{ cm}^{-2}$ and $3.5 \times 10^{11} \text{ cm}^{-2}$, respectively. When \vec{E} is applied in the perpendicular direction, interlayer exciton energy in the bilayer shifts linearly, Fig. 2a, as expected from a first-order Stark effect. Fitting the exciton peak shifts to $\Delta E_{\text{ex}} = -\vec{p} \cdot \vec{E}$ gives the interlayer exciton dipole moment of $\vec{p} = 5.7 \pm 0.1 e \cdot \text{\AA}$, in agreement with a previous report³⁰. The \vec{E} -dependent PL spectra from the trilayer exhibit two linear regions with opposite slopes that symmetrically cross at $\vec{E} = 0\text{V}$, Fig. 2b, as expected from the Stark effect for dipolar excitons confined in the top or bottom heterojunctions, respectively, with oppositely pointing dipoles. From

the slopes, we obtain $|\vec{p}| = 5.5 \pm 0.1 e \cdot \text{\AA}$ in the trilayer. Note that the dipole moments of the interlayer excitons are identical for all the sharp PL peaks in either the bilayer or trilayer, as they are all determined from the interlayer separation at vdW contacts. In contrast, the PL peak positions vary due to sample disorder and changes in local electrostatic environments.

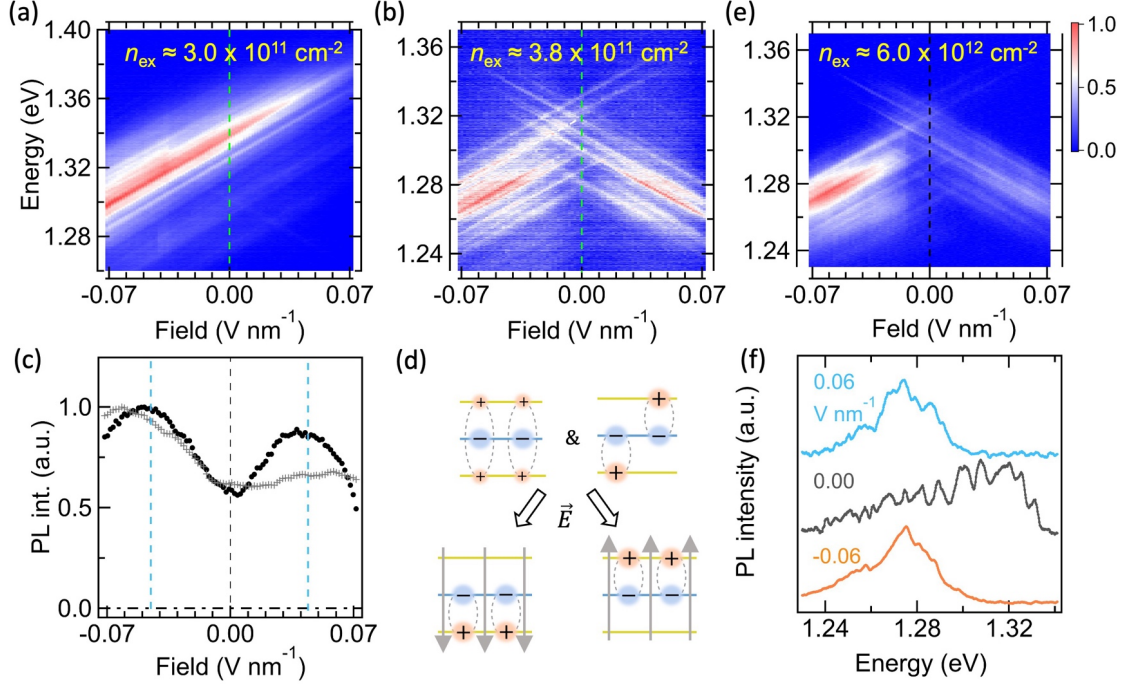


Fig. 4 | Field-dependent PL spectra in the trilayer reveal dark-to-bright excitonic transition. \vec{E} -dependent PL spectra of interlayer excitons in the WSe₂/MoSe₂ bilayer (a) and the WSe₂/MoSe₂/WSe₂ trilayer (b). The color bar represents normalized PL intensity. (d). Integrated PL intensity from the trilayer as a function of \vec{E} in the trilayer. \vec{E}_{C1} and \vec{E}_{C2} label critical field values where the integrated PL intensities peak. (e) Schematic illustration of quadrupolar to dipolar exciton transition induced by electric fields. CW excitation: $h\nu = 2.33$ eV, power $\rho = 0.17$ μ W; sample temperature $T = 4.6$ K. 5×10^{12}

Interestingly, the PL intensities from the trilayer are lower at $|\vec{E}| = 0$, increase with $|\vec{E}|$, and reach peaks at $|\vec{E}_C| = 0.045 \pm 0.003$ V·nm⁻¹, before decreasing again at $|\vec{E}| > |\vec{E}_C|$, Fig. 2c (black dots). The decrease in PL intensity with increasing $|\vec{E}|$ above $|\vec{E}_C|$ for red-shifted interlayer excitons can be understood from the decreased oscillator strength, which results from further spatial separation of the e-h pair driven by the \vec{E} field³⁰. The opposite trend seen in the region $|\vec{E}| < |\vec{E}_C|$ is unusual and suggests that optically dark species are turned into bright excitons by increasing \vec{E} . These observations are consistent with the presence of quadrupolar excitons, which

are predicted to be the most stable exciton phase and optically dark in the trilayer. This can be understood by the addition of the linear Stark effect, $-\vec{E} \sum_i \vec{p}_i$, to the system Hamiltonian in equation (2):

$$\hat{H}_{TL-E} = \sum_i (K_i) + \sum_{i<j} (V_{\uparrow\uparrow j} - V_{\uparrow\downarrow j}) - \Delta_Q \sum_i \sigma_i^x - \vec{E} \sum_i \vec{p}_i \quad (3).$$

While the Stark term is zero for either quadrupolar or staggered dipolar lattices, it can overcome both stabilization energies ($V_{\uparrow\downarrow j}$ and Δ_Q) and switch the interlayer excitons to one of the two heterojunctions to align with \vec{E} , Fig. 4d. From the experimental values of $|\vec{E}_C| = 0.045 \text{ V}\cdot\text{nm}^{-1}$, we have $\Delta E = -\vec{p} \cdot \vec{E} = -25 \text{ meV}$, which is within the range of the predicted stabilization energies of the exciton lattices^{8,10}. Note that not all excitonic species at $|\vec{E}| \sim 0$ are optically dark and the co-existence of bright dipolar excitons and dark quadrupolar excitons may be attributed the unavoidable sample heterogeneity. Note also that the PL intensity distribution is asymmetric in positive and negative \vec{E} ; this is likely a result of sample asymmetry, e.g., the more efficient quenching of excitons by the bottom graphite gate.

At $n_{\text{ex}} > n_{\text{Mott}}$ ($\sim 3 \times 10^{12} \text{ cm}^{-2}$ in the heterobilayer^{15,18}), excitons in the trilayer driven by \vec{E} to one of the two heterobilayers is expected to undergo a Mott transition. This is confirmed in Fig. 4e for the trilayer at $n_{\text{ex}} = 6.0 \times 10^{12} \text{ cm}^{-2}$, where the sharp PL peaks at $\vec{E} = 0 \text{ V}$ merge into broadened peaks as \vec{E} is swept in both directions, indicating field-driven phase transitions to electron/hole plasmas. Fig. 3f compares the PL spectra at $\vec{E} = 0, 0.6$, and -0.6 V . The sharp PL peaks of the crystalline phases at $\vec{E} = 0 \text{ V}$ broaden into spectra characteristic of the plasma phase in one of the two bilayers at $\vec{E} = 0.6$ or -0.6 V . For comparison, in the bilayer region at $n_{\text{ex}} > n_{\text{Mott}}$, the PL spectra remain broad as expected from the plasma phase in the entire range of Stark tuning; see Fig. S15 for $n_{\text{ex}} = 4.8 \times 10^{12} \text{ cm}^{-2}$. Note the critical field $|\vec{E}_C|$ for the transition from the dark quadrupolar to the bright dipolar excitons shifts to higher values at larger n_{ex} (grey dots in Fig. 4c for $n_{\text{ex}} = 6.0 \times 10^{12} \text{ cm}^{-2}$); this may be attributed to the higher cohesive energy of the quadrupolar exciton crystals at higher n_{ex} .

Concluding remarks. We present experimental evidences for ordered phases of interlayer excitons, as theoretically predicted for the symmetric $\text{WSe}_2/\text{MoSe}_2/\text{WSe}_2$ heterotrilaier. Ordered quantum phases in TMDC bilayers have been reported before only for Fermions, and our

experimental evidences for the bosonic interlayer excitons in the trilayer likely result from the increased “dimensionality” which stabilizes the ordered bosons. An intriguing question for future research is whether ordering of excitonic quasiparticles can lead to quantum coherent phenomena³¹, such as exciton condensation^{32,33} or Dicke superradiance in ordered emitter arrays^{34,35}. The study of these coherent phenomena requires the determination of the quantum nature of light from correlation analysis, which is difficult due to the low oscillator strength of interlayer excitons in the WSe₂/MoSe₂ heterojunction. In this regard, it might be beneficial to use other symmetric trilayers, such as WS₂/MoSe₂/WS₂, where hybridization of interlayer exciton with intralayer exciton gives rise to much larger oscillator strength¹⁴. These and other TMDC trilayers or multilayers may provide versatile playgrounds for the exploration of quantum phase transitions and quantum coherent phenomena of optically bright bosons.

Methods

Device fabrications. Monolayer WSe₂ and MoSe₂ were mechanically exfoliated from bulk crystals grown by the self-flux method. These monolayers feature the lowest reported defect densities ($\leq 10^{10} \text{ cm}^{-2}$)³⁶. Flakes of h-BN with thicknesses of 11-13 nm and graphite with thicknesses of $\sim 1\text{--}1.5 \text{ nm}$ ($\sim 3\text{--}4$ layers of graphene, optically transparent) were also obtained via mechanical exfoliations. The surfaces flatness (height fluctuation $< 0.5 \text{ nm}$ across the whole flake) of TMDC monolayer, h-BN flakes, and thin graphite were all characterized by atomic force microscopy (AFM).

The h-BN/Graphite (top-gate)/h-BN/WSe₂/MoSe₂/WSe₂/Graphite (contact)/h-BN/Graphite (bottom-gate)/h-BN heterostructure was prepared by the dry stamp method³⁷. Briefly, we coated a thin polycarbonate (PC) polymer film on top of a transparent polydimethylsiloxane (PDMS) cube ($\sim 1 \times 1 \times 1 \text{ mm}^3$), and used this micro-lens stamp to pick up the top h-BN flake. This h-BN was then used to pick up all the rest of the 2D flakes and monolayers one-by-one in a desired sequence. The near 0° twist angles between WSe₂ and MoSe₂ monolayers were ensured by SHG characterization (*vide infra*), and aligned via a rotation stage. A key feature of the trilayer device is structural symmetry. In order to meet this requirement, we employ the tear-and-stack approach to fabricate the heterostructure, i.e., one single sheet of WSe₂ was utilized; this WSe₂ monolayer was first teared and one of the two teared piece was picked up, followed by picking up the MoSe₂ layer,

and then the second teared piech of WSe₂ to form the WSe₂/MoSe₂/WSe₂ heterostructure (see Fig. S4 for an illustration). After picking up all the layers in the desired order, we transferred the entire heterostructure onto a clean silicon wafer at elevated temperatures (~120 – 180°C). The sample surface was then washed with chloroform, acetone, and isopropanol consecutively. The heterostructure was then patterned with metal electrode: metal gates and contacts (Cr/Pd/Au: 3nm/20nm/60nm) were evaporated (Angstrom Engineering UHV E-beam deposition system) on top of the exposed regions of the gate and contact graphite (see SI Fig. S5 for the full optical image of the device).

Determination of the TMDC monolayer crystal orientation by SHG. The detailed procedures for polarization-resolved SHG measurements were discussed in ref. ³⁸. We acquired the azimuthal angular (θ) distribution of SHG signal by rotating the laser polarization and the SHG signal (via a half waveplate) at fixed sample orientation. Due to the D_{3h} symmetry, the non-vanishing tensor elements of the second order susceptibility of WSe₂ or MoSe₂ monolayer are $\chi_{yyy}^{(2)} = -\chi_{yxx}^{(2)} = -\chi_{xxy}^{(2)} = -\chi_{xyx}^{(2)}$ where the x axis is defined as the zigzag direction.³⁸ When we simultaneously rotated the fundamental and SHG signals, the SHG intensity showed six-fold symmetry: $I_{\perp} \propto \cos^2(3\theta)$ and $I_{\parallel} \propto \sin^2(3\theta)$, where θ is the angle between the laser polarization and the zigzag direction. We fixed all substrates supporting the TMDC monolayers are onto a single glass slide; thus, the relative crystal orientations are determined directly by comparison to a triangular CVD TMDC monolayer where the zigzag directions are their crystal edges.

To perform the phase-resolved SHG measurements, Fig. S3, we employed a similar strategy as that described elsewhere^{39,40}. Prior to phase-resolved measurements, we assured that the azimuthal angles of TMDC monolayers were co-polarized (relying on the above polarization-resolved SHG measurements); however, at this stage, it remained unknown whether these co-polarized TMDC monolayers possessed 0° or 60° twist angles. Linearly polarized femtosecond laser light (Spectrum Physics Tsunami, 80 MHz, 800 nm, 80 fs) was first focused onto a thin z-cut quartz crystal (0.1 mm × 1 cm × 1 cm, MTI Corporation) by a NIR AR-Coated lens ($f = 5$ cm), which generated a 400 nm SHG reference pulse signal (SHG₁) propagating with the remaining 800 nm femtosecond pump beam. These beams were collected by an achromatic (400-1100 nm) doublet lens and collimated. A picosecond-scale time interval ($\Delta\tau$) between the SHG₁ and pump pulse existed. The beams were directed to an inverted optical microscope (Olympus IX73) where

the samples were placed. Upon the arrival and focus (NA 0.50 objective, Olympus UPLFLN 20X) of the two pulses at the TMDC monolayer sample surface, another SHG signal (SHG₂) was produced from the TMDC monolayer by the remaining 800 nm pump beam. SHG₁ and SHG₂ were collectively filtered by a short-pass filter and directed to a visible spectrometer, and further detected by an EM-CCD camera. The diffraction grating performed the time-to-frequency domain Fourier transformations for SHG₁ and SHG₂ with interval $\Delta\tau$, which was followed by the spectral interferences at the EM-CCD; the ultimate spectra from the EM-CCD showed the interference patterns. In this regard, TMDC monolayers having a θ initial azimuthal angle vs. that having a $\theta+60^\circ$ azimuthal angle displayed alternating interference patterns as shown in SI, Fig. S2.

Electric field and doping. The analysis about e

Electric field application and electrostatic doping in a parallel dual-gate device were discussed in details previously⁴¹. The equivalent circuit of our dual-gate device was a parallel plate capacitor with a 2D sheet of material (i.e., the TMDC heterostructure) in the middle. We define the thickness of the top insulating h-BN in between the TMDC heterostructure and the top graphite gate as d_1 (≈ 11 nm), and the bottom one as d_2 (≈ 13 nm). The dielectric constants for h-BN and TMDC are $\epsilon_{h-BN} \approx 3.9$, and $\epsilon_{TMDC} \approx 7.2$.⁴¹⁻⁴³ Then, the electric field generated in between the top and bottom gates can be expressed as

$$|\vec{E}| = \frac{V_{tg} - V_{bg}}{d_1 + d_2} / \left(\frac{\epsilon_{TMDC}}{\epsilon_{h-BN}} + \frac{d_{HS}}{d_1 + d_2} \right) \quad (4)$$

where V_{tg} and V_{bg} are the top and bottom gate voltages, respectively; d_{HS} is the thickness of the TMDC heterostructure. The doping in the middle 2D sheet material (i.e., TMDC trilayer) is

$$ne \approx C_1 V_{tg} + C_2 V_{bg} - n_0 e \approx \frac{\epsilon_{h-BN} \cdot A}{d_1} V_{tg} + \frac{\epsilon_{h-BN} \cdot A}{d_2} V_{bg} - n_0 e \quad (5)$$

where n is the doping density, C_1 (C_2) is the capacitance from the capacitor formed by the top (bottom) graphite gate and the TMDC sheet, A is the capacitor area, and n_0 is the in-gap state density that need to be filled before the conduction (valence) band is filled with electrons (holes).

We control the electric field and electrostatic doping independently: (1) if $V_{tg} = -\frac{d_1}{d_2} V_{bg}$, there will be no external doping effect, and $|\vec{E}|$ scales linearly with $V_{tg} - V_{bg}$; (2) if $V_{tg} = V_{bg}$, there will be no external electric field, and doping density scales linearly with V_g ($= V_{tg} = V_{bg}$).

Additionally, we treat the energy shift (ΔE) of dipolar excitons in an electric field based on the first-order Stark effect,

$$\Delta E = -\vec{p} \cdot \vec{E} \quad (6)$$

where $\vec{p} = e \cdot \vec{d}$, \vec{d} is the interlayer separation between two TMDC monolayers with the direction pointing from the negative to positive charge. This enabled us to estimate the electron-hole separation to be $\sim 6\text{\AA}$ based on the \vec{E} -dependent PL spectra.

Photoluminescence microscopy/spectroscopy. The gate-dependent PL spectra measurements were performed on a home-built spectro-microscopic system³⁸ based on a liquid-helium recirculating optical cryostat (Montana Instruments Fusion/X-Plane) with a 100x, NA 0.75 objective (Zeiss LD EC Epiplan-Neofluar 100x/0.75 HD DIC M27). The temperature of the sample stage could be varied between 3.8 K and 350 K. In all experiments presented in this study, the TMDC heterobilayer and monolayers samples were at 4 K in a vacuum ($<10^{-6}$ torr) environment, unless otherwise noted. The incident laser beam (Coherent Rega, 750 nm, ~ 150 fs, 76 MHz) was focused by the objective to a diffraction limited spot on the sample. The excitation power was measured by a calibrated power meter (Ophir StarLite) with broad dynamic range. The PL light was collected by the same objective, spatially and spectrally filtered, dispersed by a grating, and detected by an InGaAs photodiode array (Princeton Instruments PyLoN-IR). The wavelength was calibrated by neon-argon and mercury atomic emission sources (Princeton Instruments IntelliCal). In all PL measurements, we found no laser heating of the sample under cryogenic cooling. The PL spectra are completely reproducible following repeated measurements at the same spot on the sample. The sample was grounded during the measurements. Gate voltages were supplied via two identical source meters (Keithley 2400, source accuracy $\sim 0.02\%$) which were computer controlled through a GPIB bus.

References

1. Wang, L. *et al.* Correlated electronic phases in twisted bilayer transition metal dichalcogenides. *Nature Materials* **19**, 861–866 (2020).
2. Xu, Y. *et al.* Correlated insulating states at fractional fillings of moiré superlattices. *Nature* **587**, 214–218 (2020).
3. Shimazaki, Y. *et al.* Strongly correlated electrons and hybrid excitons in a moiré heterostructure. *Nature* **580**, 472–477 (2020).

4. Tang, Y. *et al.* Simulation of Hubbard model physics in WSe₂/WS₂ moiré superlattices. *Nature* **579**, 353–358 (2020).
5. Regan, E. C. *et al.* Mott and generalized Wigner crystal states in WSe₂/WS₂ moiré superlattices. *Nature* **579**, 359–363 (2020).
6. Smoleński, T. *et al.* Signatures of Wigner crystal of electrons in a monolayer semiconductor. *Nature* **595**, 53–57 (2021).
7. Zhou, Y. *et al.* Bilayer Wigner crystals in a transition metal dichalcogenide heterostructure. *Nature* **595**, 48–52 (2021).
8. Slobodkin, Y. *et al.* Quantum Phase Transitions of Trilayer Excitons in Atomically Thin Heterostructures. *Physical Review Letters* **125**, 255301 (2020).
9. Sammon, M. & Shklovskii, B. I. Attraction of indirect excitons in van der Waals heterostructures with three semiconducting layers. *Physical Review B* **99**, 165403 (2019).
10. Astrakharchik, G. E., Kurbakov, I. L., Sychev, D. V., Fedorov, A. K. & Lozovik, Y. E. Quantum phase transition of a two-dimensional quadrupolar system. *Physical Review B* **103**, L140101 (2021).
11. Seyler, K. L. *et al.* Signatures of moiré-trapped valley excitons in MoSe₂/WSe₂ heterobilayers. *Nature* **567**, 66–70 (2019).
12. Tran, K. *et al.* Evidence for moiré excitons in van der Waals heterostructures. *Nature* **567**, 71–75 (2019).
13. Bai, Y. *et al.* Excitons in strain-induced one-dimensional moiré potentials at transition-metal dichalcogenide heterojunctions. *Nature Materials* **19**, 1068–1073 (2020).
14. Alexeev, E. M. *et al.* Resonantly hybridized excitons in moiré superlattices in van der Waals heterostructures. *Nature* **567**, 81–86 (2019).
15. Wang, J. *et al.* Diffusivity Reveals Three Distinct Phases of Interlayer Excitons in MoSe₂/WSe₂ Heterobilayers. *Physical Review Letters* **126**, 106804 (2021).
16. Sondhi, S. L., Girvin, S. M., Carini, J. P. & Shahar, D. Continuous quantum phase transitions. *Rev Mod Phys* **69**, 315 (1997).
17. Lagoin, C., Suffit, S., Baldwin, K., Pfeiffer, L. & Dubin, F. Mott insulator of strongly interacting two-dimensional semiconductor excitons. *Nature Physics* **18**, 149–153 (2022).
18. Wang, J. *et al.* Optical generation of high carrier densities in 2D semiconductor heterobilayers. *Sci Adv* **5**, eaax0145 (2019).
19. Wigner, E. On the interaction of electrons in metals. *Physical Review* **46**, 1002 (1934).
20. Wu, F., Lovorn, T., Tutuc, E. & Macdonald, A. H. Hubbard Model Physics in Transition Metal Dichalcogenide Moiré Bands. *Physical Review Letters* **121**, 26402 (2018).
21. Kennes, D. M. *et al.* Moiré heterostructures as a condensed-matter quantum simulator. *Nature Physics* **17**, 155–163 (2021).
22. Yao, W., Xu, X., Liu, G.-B., Tang, J. & Yu, H. Moiré excitons: From programmable quantum emitter arrays to spin-orbit-coupled artificial lattices. *Science Advances* **3**, e1701696 (2017).
23. Gu, J. *et al.* Dipolar excitonic insulator in a moiré lattice. *Nature Physics* **18**, 395–400 (2022).
24. Zhang, Z. *et al.* Correlated interlayer exciton insulator in double layers of monolayer WSe₂ and moiré WS₂/WSe₂. *arXiv preprint arXiv:2108.07131* (2021).
25. Zeng, Y. *et al.* Exciton density waves in Coulomb-coupled dual moiré lattices. *arXiv preprint arXiv:2205.07354* (2022).

26. Edelberg, D. *et al.* Approaching the Intrinsic Limit in Transition Metal Diselenides via Point Defect Control. *Nano Letters* **19**, 4371–4379 (2019).
27. Yu, H., Wang, Y., Tong, Q., Xu, X. & Yao, W. Anomalous light cones and valley optical selection rules of interlayer excitons in twisted heterobilayers. *Phys Rev Lett* **115**, 187002 (2015).
28. Li, W., Lu, X., Dubey, S., Devenica, L. & Srivastava, A. Dipolar interactions between localized interlayer excitons in van der Waals heterostructures. *Nature Materials* **19**, 624–629 (2020).
29. Baek, H. *et al.* Highly energy-tunable quantum light from moiré-trapped excitons. *Sci Adv* **6**, eaba8526 (2020).
30. Jauregui, L. A. *et al.* Electrical control of interlayer exciton dynamics in atomically thin heterostructures. *Science* **366**, 870–875 (2019).
31. Boening, J., Filinov, A. & Bonitz, M. Crystallization of an exciton superfluid. *Physical Review B* **84**, 75130 (2011).
32. Wang, Z. *et al.* Evidence of high-temperature exciton condensation in two-dimensional atomic double layers. *Nature* **574**, 76–80 (2019).
33. Sigl, L. *et al.* Signatures of a degenerate many-body state of interlayer excitons in a van der Waals heterostack. *Physical Review Research* **2**, 42044 (2020).
34. Masson, S. J., Ferrier-Barbut, I., Orozco, L. A., Browaeys, A. & Asenjo-Garcia, A. Many-body signatures of collective decay in atomic chains. *Physical Review Letters* **125**, 263601 (2020).
35. Rainò, G. *et al.* Superfluorescence from lead halide perovskite quantum dot superlattices. *Nature* **563**, 671 (2018).
36. Kim, B. *et al.* Free Trions with Near-Unity Quantum Yield in Monolayer MoSe₂. *ACS Nano* aacs.nano.1c04331 (2021) doi:10.1021/acsnano.1c04331.
37. Wang, L. *et al.* One-Dimensional Electrical Contact to a Two-Dimensional Material. *Science* (1979) **342**, 614–617 (2013).
38. Bai, Y. *et al.* Excitons in strain-induced one-dimensional moiré potentials at transition metal dichalcogenide heterojunctions. *Nature Materials* **19**, 1068–1073 (2020).
39. Schaibley, J. R. *et al.* Directional interlayer spin-valley transfer in two-dimensional heterostructures. *Nature Communications* **7**, (2016).
40. Nelson, C. A. *et al.* Time-, energy-, and phase-resolved second-harmonic generation at semiconductor interfaces. *Journal of Physical Chemistry C* **118**, 27981–27988 (2014).
41. Jauregui, L. A. *et al.* Electrical control of interlayer exciton dynamics in atomically thin heterostructures Downloaded from. *Science* (1979) **366**, 870–875 (2019).
42. Laturia, A., van de Put, M. L. & Vandenberghe, W. G. Dielectric properties of hexagonal boron nitride and transition metal dichalcogenides: from monolayer to bulk. *npj 2D Materials and Applications* **2**, 6 (2018).
43. Kim, K. *et al.* Band alignment in WSe₂-graphene heterostructures. *ACS Nano* **9**, 4527–4532 (2015).

Acknowledgements. This work was supported by the Materials Science and Engineering Research Center (MRSEC) through NSF grant DMR-2011738. Partial support for sample fabrication by the Vannevar Bush Faculty Fellowship through the Office of Naval Research

through Grant No. N00014-18-1-2080 is also acknowledged. We thank Andrew Millis, Ana Asenjo-Garcia, Xiaodong Xu, and Farhan Rana for fruitful discussions and Wenjing Wu for help with sample preparation at the initial stage of this project.

Data Availability. The data represented in Figs. 1-4 are provided with the article source data. All data that support the results in this article are available from the corresponding author upon reasonable request.

Author contributions:

YB and XYZ conceived this work. YB carried out all experiments with assistance by SL, YG, JP, JW, CRD, and JH. XYZ supervised the project. The manuscript was prepared by YJB and XYZ in consultation with all other authors. All authors read and commented on the manuscript.

Competing Interests. All authors declare that they have no competing interests.

Supporting Information

Evidence for Exciton Crystals in a 2D Semiconductor Heterotrilaier

Yusong Bai,¹ Song Liu,² Yinjie Guo,³ Jordan Pack,³ Jue Wang,¹ Cory R. Dean,³ James Hone,² X.-Y. Zhu^{1,†}

[†] To whom correspondence should be addressed: xyzhu@columbia.edu

4. Department of Chemistry, Columbia University, New York, NY 10027, USA.
5. Department Mechanical Engineering, Columbia University, New York, NY 10027, USA.
6. Department of Physics, Columbia University, New York, NY, 10027, USA.

I. Supplementary Figures

Fig. S1 | TMDC monolayer optical images and polarization-resolved SHG.

Fig. S2 | Phase-resolved SHG.

Fig. S3 | SHG optical apparatus.

Fig. S4 | Schematic illustration the WSe₂/MoSe₂/WSe₂ pickup process.

Fig. S5 | Optical image for the overview of the device.

II. Supplementary Text

1. Optical excitation density estimation.

Fig. S6 | Schematic illustration of device architecture in the side view.

Fig. S7 | Complex refractive indices for Graphene (left), h-BN (middle), and WSe₂ (right).

Fig. S8 | Calibration of steady-state excitation density.

2. Temperature-dependent PL spectra

Fig. S9 | Temperature-dependent and power-dependent PL spectra.

Fig. S10 | Temperature-dependent PL spectra.

3. Power-dependent diffusion experiments.

Fig. S11 | Steady-state diffusion experiments at increasing excitation densities.

Fig. S12 | Fitting of PL intensity image.

Fig. S13 | Experimental determination of the point spread function (PSF).

Fig. S14 | Estimation of diffusion constants.

4. Field-dependent PL spectra of the bilayer

Fig. S15 | Field-dependent PL spectra of WSe₂/MoSe₂.

I. Supplementary Figures.

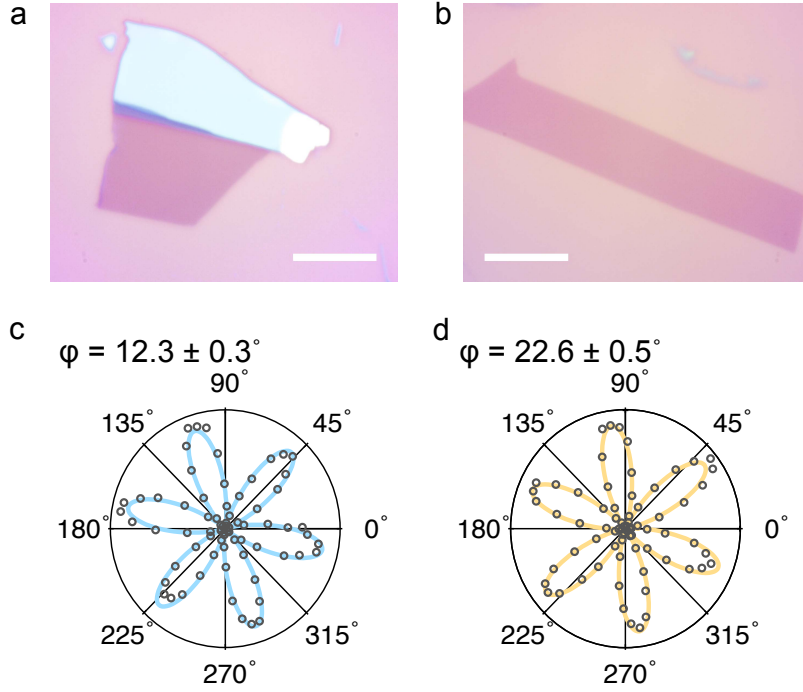


Fig. S1 | TMDC monolayer optical images and polarization-resolved SHG. (a)-(b) Optical images for the MoSe₂ (a) and WSe₂ (b) monolayers used in fabricating the heterostructure devices. Scalebar is 10 μm . (c)-(d) the polarization-resolved SHG data (circles) and fit (lines) of MoSe₂ (c) and WSe₂ (d) monolayers.

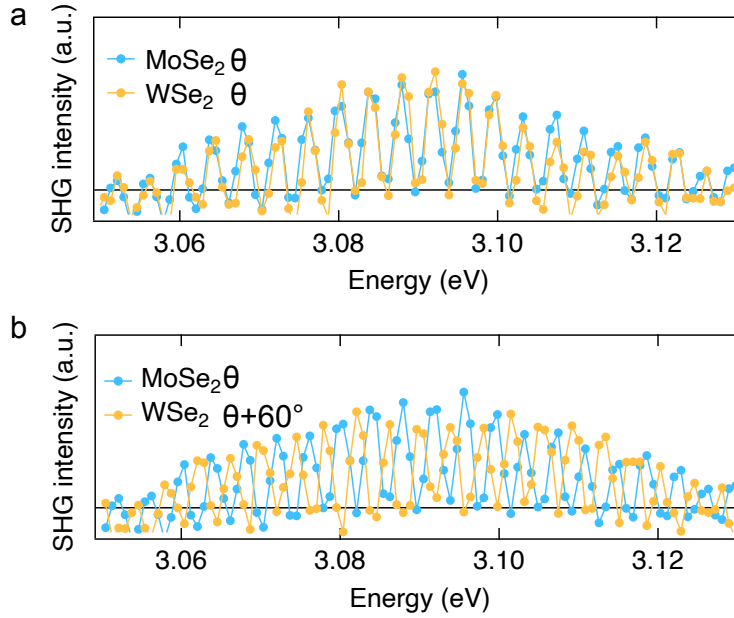


Fig. S2 | Phase-resolved SHG. (a) SHG interference spectra from Monolayer MoSe₂ (blue) or WSe₂ (yellow) and from the front surface of z-cut quartz. In this case, the MoSe₂, WSe₂, and the

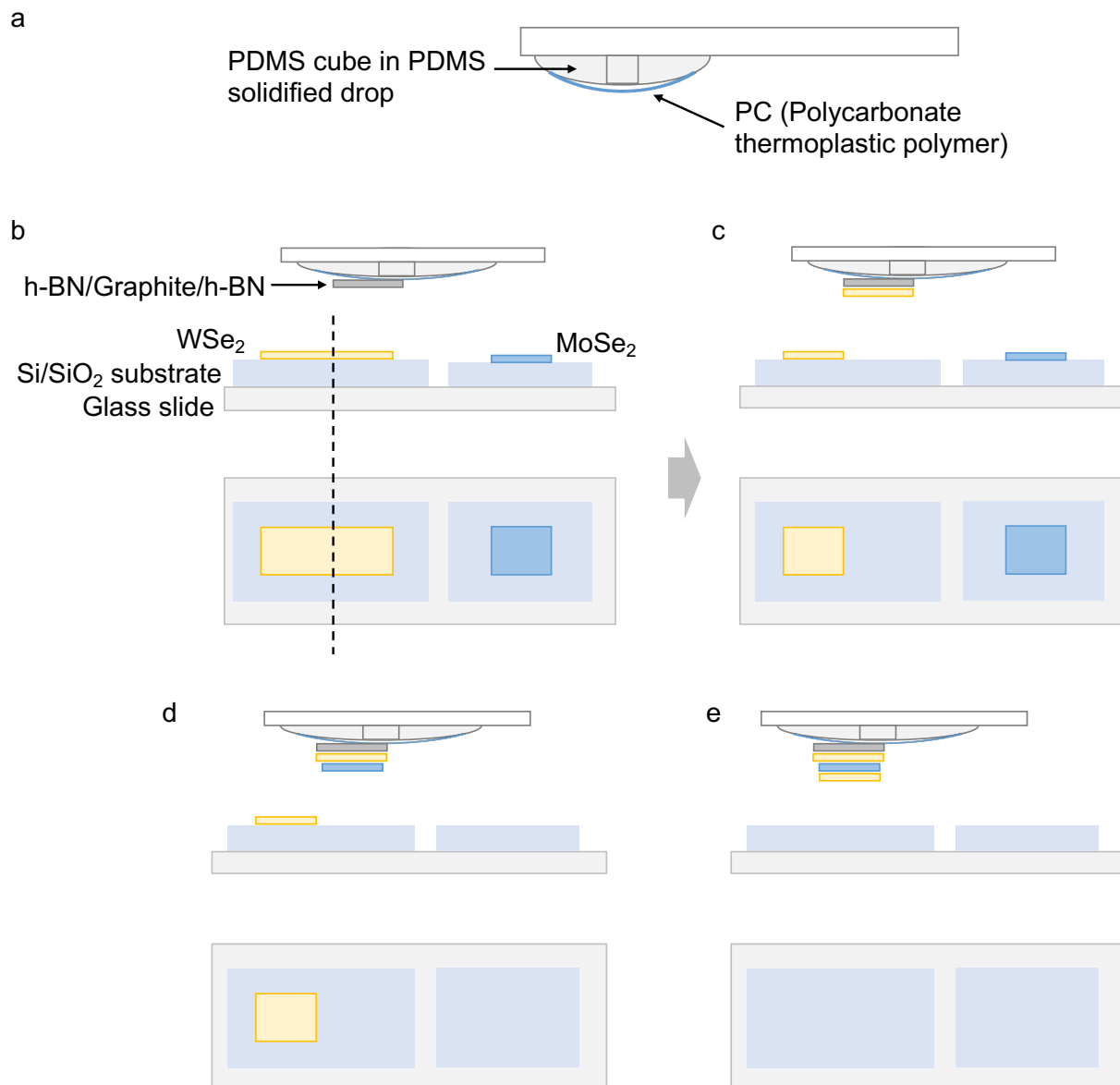


Fig. S4 | Schematic illustration the WSe₂/MoSe₂/WSe₂ pickup process. (a) The pick-up for transferring 2D monolayers. (b)-(c) Tear-and-pickup of the WSe₂ monolayer. This is enabled by a h-BN having a sharp edge. (d)-(e) Stack of the MoSe₂ and the rest half of the WSe₂ monolayers. Note that, in this process the top and bottom WSe₂ layers in the trilayer heterostructure come from the same monolayer and there is no relative rotation comparing step (b) to step (d); such a protocol enables the formation of a symmetric trilayer structure.

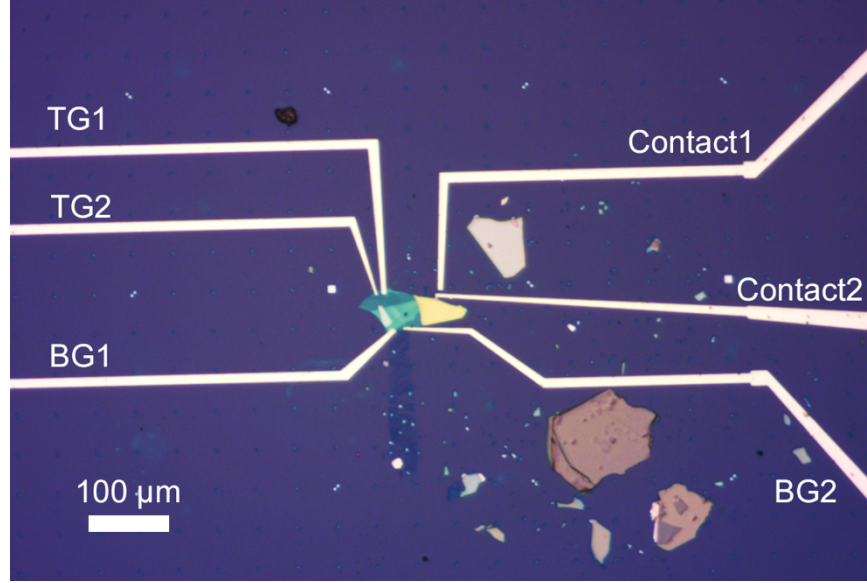


Fig. S5 | Optical image for the overview of the device. WSe₂/MoSe₂/WSe₂ trilayer heterostructure device with double gates and contacts. TG: top gate; BG: bottom gate.

II. Supplementary Text.

1. Optical excitation density estimation. We previously have detailed the protocols for estimating the optical excitation densities for h-BN encapsulated WSe₂/MoSe₂ heterostructures¹. The current device sample differs from the previously exploited samples in two major aspects: (1) the increase in the absorptance in the trilayer heterostructure (WSe₂/MoSe₂/WSe₂) compared to that in the bilayer region (WSe₂/MoSe₂) due to the additional WSe₂ layer, and (2) the attenuation of incident excitation beams due to the inclusion of few-layer graphene (graphite, ~ 1.035 nm) top gate. For point (1), we estimate the absorptance of WSe₂/MoSe₂/WSe₂ based on the dielectric functions of WSe₂ and MoSe₂ measured by Li et al.², where the absorptance of WSe₂ at 532 nm is $A_W(532\text{ nm}) \approx 7.7\%$, and that for MoSe₂ is $A_M(532\text{ nm}) \approx 12.3\%$.

Regarding point (2), knowing the complex refractive index for a material, i.e., $\tilde{n}(\lambda) = n(\lambda) - i\kappa(\lambda)$ (n is the real part of the refractive index, indicating phase velocity; κ is the imaginary part, indicating the attenuation of the wave propagating through the medium; n and κ are functions of wavelength λ), the transmittance of the beam at a wavelength can be calculated based on $T = 1 - R - A$, where R is the reflectance, and A is the absorptance. Fig. S9 illustrates

the major four mediums where the incident beam passes through, including vacuum (n_1), few-layer graphene (n_2), h-BN (n_3) and TMDC layers (n_4). The graphite layer contributes to power loss by both reflection (reflectance R_G) and absorption (absorptance A_G), while h-BN is a large-bandgap insulator and leads to power loss mainly through reflection (reflectance R_{BN}). Therefore, the fraction of power delivered to TMDC could be estimated based on

$$T(\lambda) = (1 - R_G - A_G) \cdot (1 - R_{G-BN}) \cdot (1 - R_{BN-TMDC}) \quad (1)$$

where R_{G-BN} is the reflection at the interface of graphite and h-BN, and $R_{BN-TMDC}$ is the reflection at the interface between h-BN and TMDC.

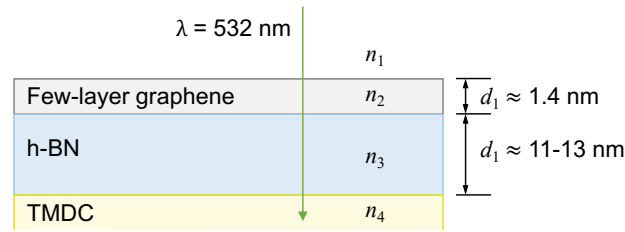


Fig. S6 | Schematic illustration of device architecture in the side view. n_1 to n_4 denote the refractive indices of vacuum, few-layer graphene, h-BN, and TMDC (WSe_2), respectively.

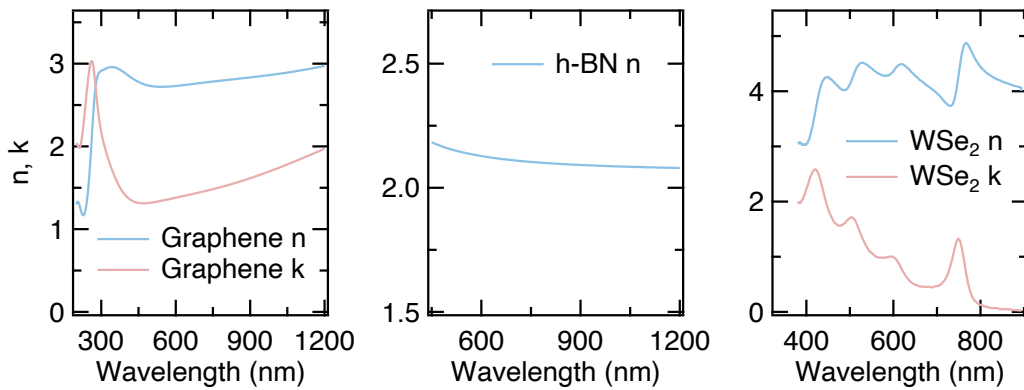


Fig. S7 | Complex refractive indices for Graphene (left), h-BN (middle), and WSe₂ (right). Note that, due to the large bandgap of h-BN, its imaginary part refractive index is not shown. All Data are adapted from refs. 2, 3, and 4.

Surface reflections with a normal incidence can be calculated based on Fresnel equation,

$$R(\lambda) = \left| \frac{n_R(\lambda) - n_T(\lambda)}{n_R(\lambda) + n_T(\lambda)} \right|^2 \quad (2)$$

where n_R is the real refractive index of the medium on the incidence side, while n_T is the real refractive index of the medium on the transmittance side. On the other hand, the absorptance is given by

$$A = 1 - e^{-\int_0^d \alpha(\lambda, z) dz} \quad (3)$$

where $\alpha(\lambda)$ is the attenuation coefficient with $\alpha(\lambda) = \frac{4\pi\kappa(\lambda)}{\lambda}$. For a material with thickness of d having a uniform absorption $A = 1 - e^{-\alpha(\lambda) \cdot d}$. Thus, knowing the complex refractive index for graphene³, and the real refractive indices of h-BN⁴ and WSe₂ monolayer⁵ (Fig. S10), we could estimate that $T(\lambda = 532nm) \approx 64.26\%$. We note that the upper bound of the excitation power density used here has not reached the absorption saturation threshold for graphene/graphite⁶, and absorption saturation effect for graphene is not considered when calculating $\alpha(\lambda)$. The calibration curves for density estimations in the bilayer and trilayer device structures are presented in Fig. S11.

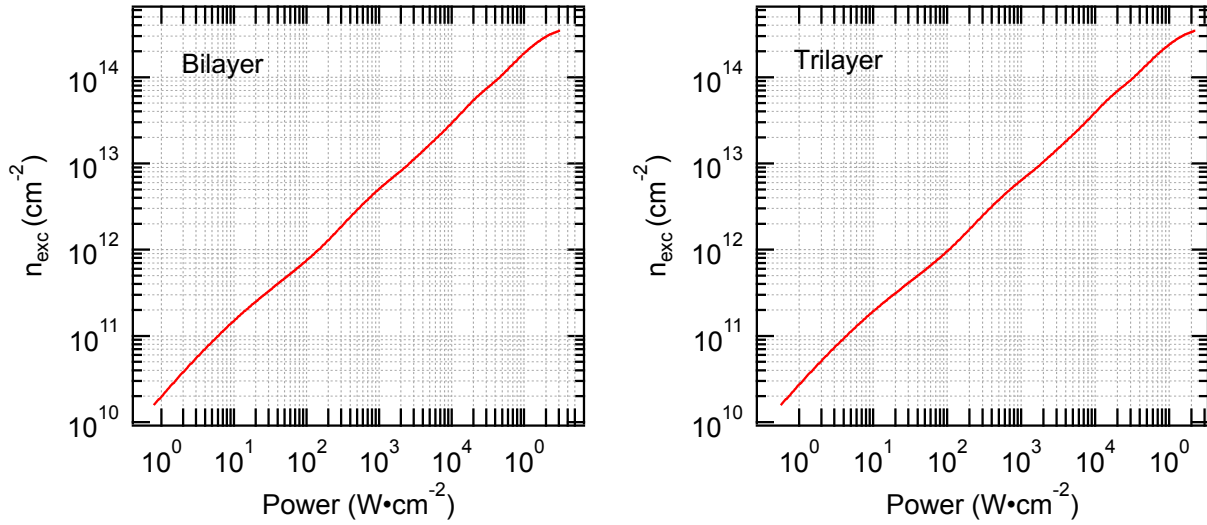


Fig. S8 | Calibration of steady-state excitation density. The calibration curves of excitation density for bilayer (left) and trilayer (right) device structures.

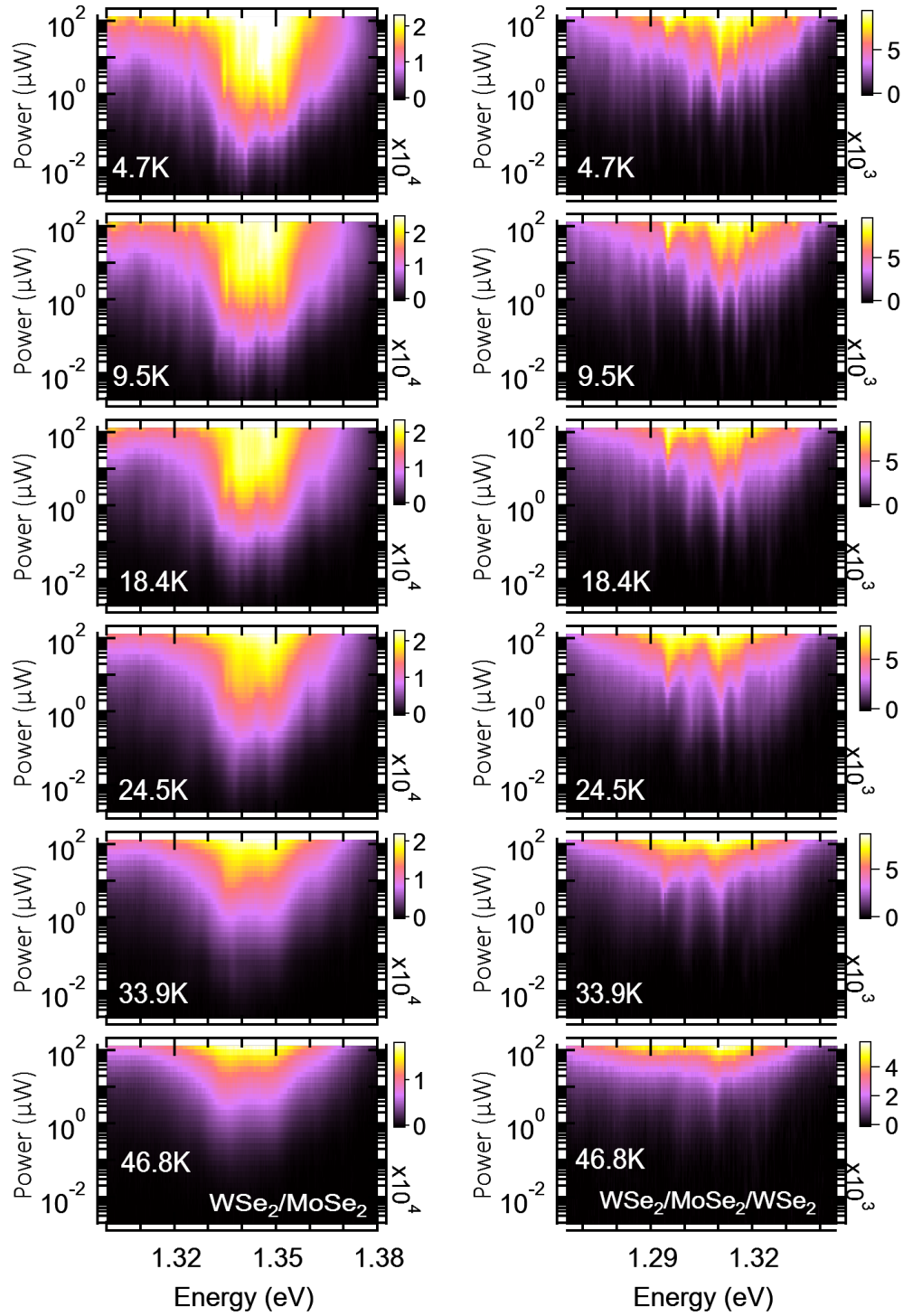


Fig. S9 | Temperature-dependent and power-dependent PL spectra. The left column shows the power-dependent spectra for WSe₂/MoSe₂ at varying temperatures, while the right column corresponds to that of the WSe₂/MoSe₂/WSe₂ heterostructure. The spectra were obtained with CW excitation at $h\nu = 2.33$ eV.

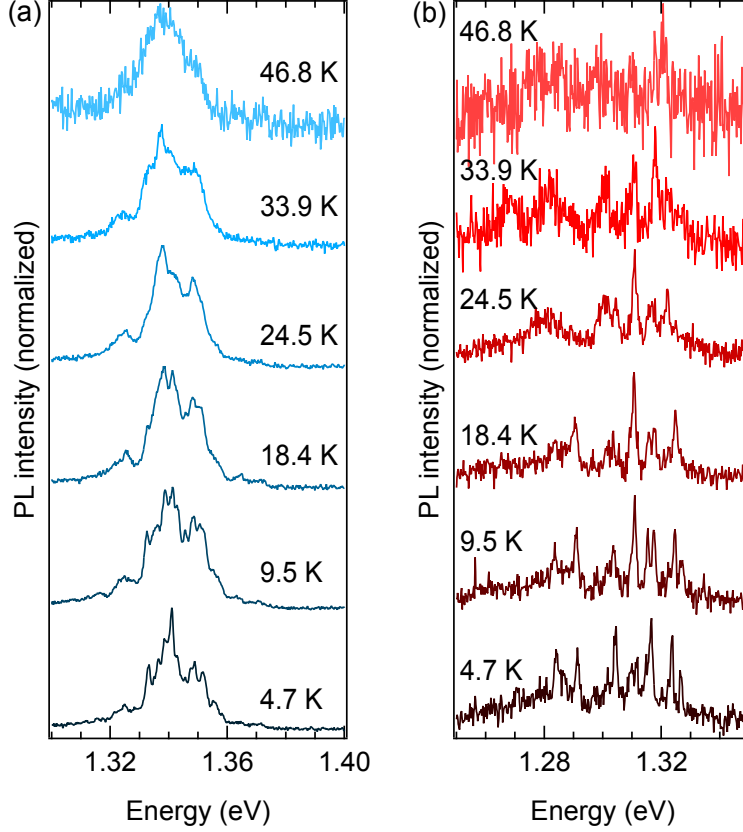


Fig. S10 | Temperature-dependent PL spectra. (a)-(b) Temperature-dependent PL spectra for the bilayer (a) and trilayer (b) heterostructures. $h\nu = 2.33$ eV, $n_{ex} \approx 1.1 \times 10^{11}$ cm⁻². Note that, at $T = 24.5$ K, the PL peaks corresponding to the trilayer heterostructure remain well resolved, while those corresponding to the bilayer heterostructure have broadened such that individual peaks are indistinguishable.

2. Power-dependent diffusion experiments. For the diffusion experiment, we employ a spatially-fixed CW excitation laser beam spot with a center wavelength at 532 nm, and collected spatially-resolved PL signal via a scanning Galvo system at increasing excitation densities. Such power-dependent diffusion results for the bilayer and trilayer heterostructures are presented in Fig. S12. To obtain the interlayer exciton variance (σ_{IX}^2), the averaged radial distances to the global centroid in each diffusion spot (Fig. S12) is fitted with a Gaussian function, $g(x) = A \cdot e^{-\frac{(x-\mu)^2}{2\sigma_{IX}^2}}$. Fig. S13 shows such an example for acquiring σ_{IX}^2 based on the data from Fig. S12-a.

The point spread function (PSF) limit (σ_0) was estimated using a white light source in the range of 900-950 nm (supercontinuum generated by Ti:sapphire) as the standard. Fig. S14 presents the spatial profile for such a standard beam spot, and the fitted σ_0 ($\sim 0.4 \mu\text{m}$); this is in close agreement with the theoretical limit of the PSF, which is $\sigma_{PSF}^* \approx 0.21 \cdot \frac{\lambda_{Em}}{NA} \approx 0.3 \mu\text{m}$ ⁷. Then, $\sigma_{IX}^2 - \sigma_0^2$ is the mean squared distance travelled by the excitons⁸. Knowing distances travelled by excitons and the excitation density-dependent PL lifetimes (Fig. S15a)⁹, the diffusion constants can also be estimated, as shown in Fig. S15b.

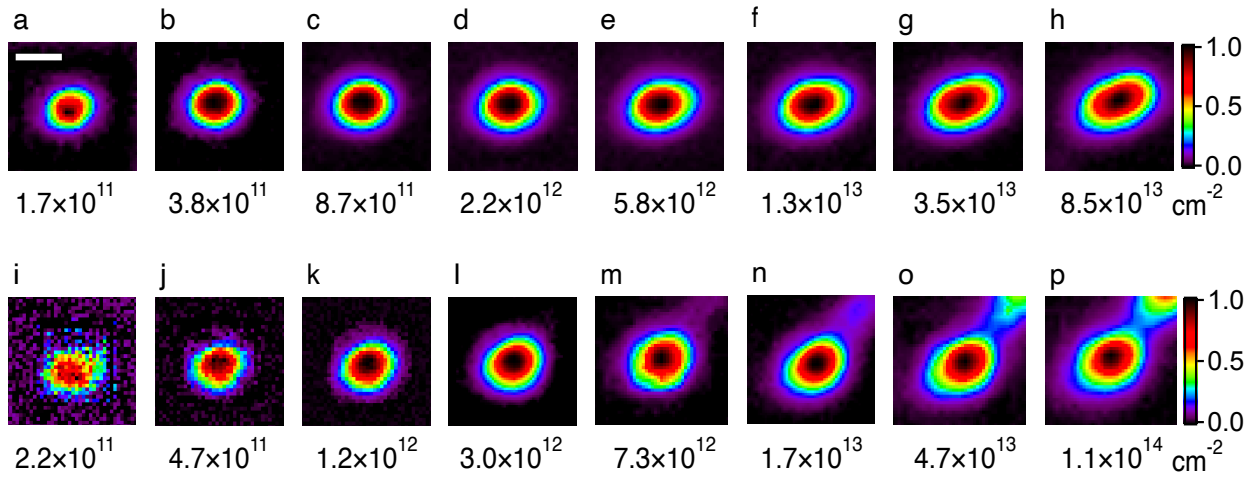


Fig. S11 | Steady-state diffusion experiments at increasing excitation densities. (a)-(h) Imaging of PL intensity for WSe₂/MoSe₂ heterostructure at different excitation densities, as noted at the bottom of each image. (i)-(p) Imaging of PL intensity for WSe₂/MoSe₂/WSe₂ heterostructure. Scalebar, $2 \mu\text{m}$.

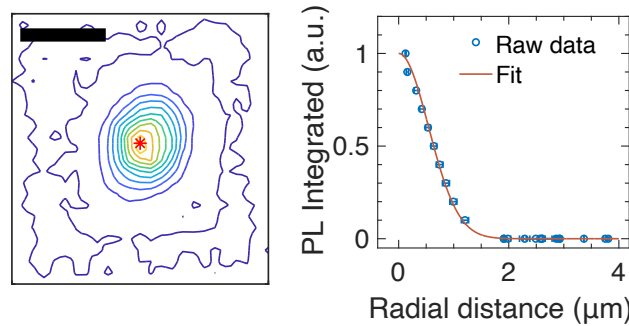


Fig. S12 | Fitting of PL intensity image. The contour plot of PL imaging (left, scalebar $2 \mu\text{m}$) and the Gaussian-function fit of average radial distances to the global centroid, based on data

shown in Fig. S10-a. The global centroid is denoted by red * symbol (left); the open circle with error bars on the right figure represents the averaged radial distances of each contour to the centroid, which is fitted with a Gaussian function (red solid line).

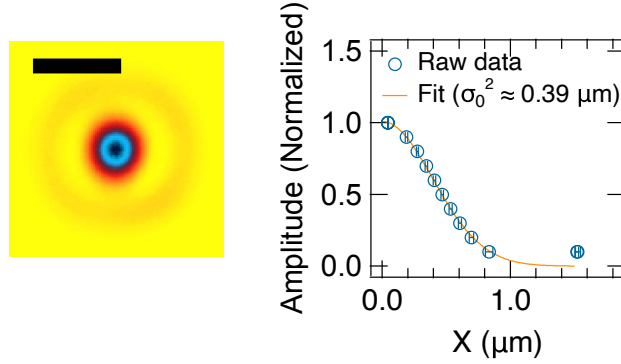


Fig. S13 | Experimental determination of the point spread function (PSF). The beam profile of a white light in the range of 900-950 nm (left, scalebar, $2 \mu\text{m}$) and the Gaussian function fit of the average radial distances to the beam center (right).

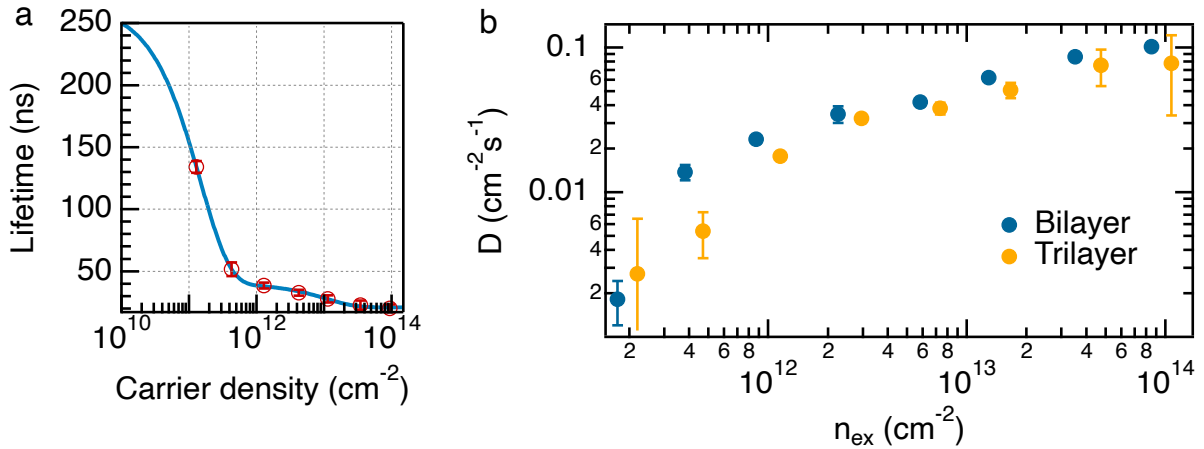


Fig. S14 | Estimation of diffusion constants. (a) The excitation density-dependent PL lifetimes for interlayer excitons (WSe₂/MoSe₂, red open circles) and apparent bi-exponential fit (blue solid line)⁹. (b) Estimated diffusion constants for interlayer excitons in the bilayer and trilayer regions.

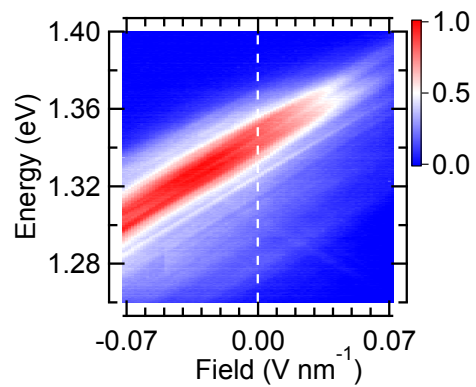


Fig. S15 | Field-dependent PL spectra of WSe₂/MoSe₂. Electric-field dependence of the PL spectra for WSe₂/MoSe₂ under an excitation density of $\sim 4.8 \times 10^{12} \text{ cm}^{-2}$. $h\nu = 2.33 \text{ eV}$, $T = 4.6 \text{ K}$.